Check for updates

Ultra-responsive and highly sensitive 1D ZnO nanotubes for detecting perilous low levels of NO$_2$ gas†

Prasad R. Godse,[a] Sujit A. Kadam, (ID) *[b] Tanaji M. Nimbalkar,[a] Yogesh M. Jadhav,[a] Yuvraj B. Jadhao,[c] Yuan-Ron Ma (ID) [b] and Vikas B. Patil (ID) *[a]

1D ZnO nanotubes were synthesized using a combination of chemical bath deposition (CBD) and thermal methods. The resulting ZnO nanotubes maintained a hexagonal crystal structure with an average length of 500–700 nm. The 1D ZnO nanotube sensor developed in this study exhibited remarkable responses of 84% for 5 ppm and 20% for 1 ppm NO$_2$ at a relatively low operating temperature of 200 °C, significantly below the exposure limit of 20 ppm. Additionally, the 1D ZnO nanotube sensor demonstrated rapid response times of 1 second for 1 ppm NO$_2$ and 2.85 seconds for 5 ppm NO$_2$. The superior performance of the 1D ZnO nanotube sensor, when compared to those of nanoparticles and broken nanotubes, can be attributed to its higher surface area, enhanced charge transport, and improved sensitivity in gas sensing applications. Impedance spectroscopy was employed to investigate the mechanism responsible for the increase in resistance due to NO$_2$ gas molecule adsorption on ZnO nanotubes. Consequently, 1D ZnO nanotubes exhibit significant potential for the development of advanced gas sensing devices.

1. Introduction

Rapid industrial expansion and vehicle emissions have led to the release of various hazardous gases into the environment, resulting in a range of health consequences.[1–6] Some of the most common polluting gases include hydrogen disulfide (H$_2$S), nitrogen dioxide (NO$_2$), acetone, and ammonia (NH$_3$).[7–10] These gases have considerable health repercussions and are significant contributors to lung diseases like emphysema, respiratory irritation syndrome, and chronic obstructive pulmonary disease.[11–13] In particular, NO$_2$ is a highly toxic gas and is a major contributor to air pollution.[14,15] Prolonged exposure to high levels of NO$_2$ can cause respiratory problems, such as bronchitis and asthma, and may even lead to lung cancer.[14,16–18] The World Health Organization (WHO) has conducted extensive research on the health risks associated with NO$_2$ emissions and has included NO$_2$ as one of the harmful pollutants in its air pollution standards for higher concentrations.[19] Exposure to high levels of NO$_2$ can lead to respiratory problems and other health issues, underscoring the importance of being able to detect and monitor its concentration in air.[20] The allowable NO$_2$ exposure level is 5–25 ppm, as per the most recent Occupational Safety and Health Administration regulations.[7,21,22] In the environment, NO$_2$ may mix with oxygen, water, and other compounds to create acid rain.[14,23] This can have detrimental effects on the stability of ecosystems. Therefore, there is a critical need for efficient NO$_2$ gas sensors that can identify and measure low amounts of NO$_2$ in the atmosphere.

Metal oxide semiconductor (MOS) resistance gas sensors are commonly used as sensing devices due to their simplicity, compact size, rapid and dependable response and exceptional sensitivity.[19,24,25] Various MOS materials have been reported as NO$_2$ sensors, including Nb$_2$O$_5$,[26] CuO,[27] NiO,[28] SnO$_2$,[29] In$_2$O$_3$,[30] CeO$_2$,[31] WO$_3$,[32,33] and Fe$_2$O$_3$.[34] However, their selectivity and response were poor at a working temperature of 200 °C. Among the range of MOS materials, ZnO emerges as a standout candidate for sensing applications. Its advantages include a large band gap (3.37 eV), widespread availability, and straightforward synthesis. Additionally, ZnO shows good electron mobility, inherent sensing capabilities, and robust electrical properties and offers the most diverse range of nanostructures.[35–41] Furthermore, it has drawn the attention of many researchers due to its excellent ability to detect NO$_2$ gas. A comparison of NO$_2$ responses of ZnO-based sensors with those of other

[a] *Functional Materials Research Laboratory, School of Physical Sciences, Solapur University, Solapur, Maharashtra 413255, India. E-mail: drvbpatil@gmail.com, vbpatil@sus.ac.in*

[b] *Department of Physics, National Dong Hwa University, Hualin 97401, Taiwan. E-mail: ksujit17@gmail.com*

[c] *Goverment College of Arts and Science, Chh. Sambhajinagar 431005*

Table 1 NO_2 responses of ZnO-500 nanotubes compared to those of other materials described in the literature

Materials	Synthesis method	Morphology	Operating temperature (°C)	NO_2 concentration (ppm)	Gas response (%)	Response time (s)	Recovery time (s)	Ref.
WO_3	Hydrothermal	Nanoflowers	200	1	6.78			32
SnO_2	Thermal evaporation	Nanoparticles	200	5	31	9.0	135	29
NiO	Chemical spray pyrolysis	Pores	200	20	57.3	—	—	28
Nb_2O_5–SE	Sol–gel method	Spherical grains	780	50	14			26
CuO	Electrospinning method	Nanofibers	150	1	4	18	3	27
ZnO	Hydrothermal	Nanosheets	170	50	10.2	36	4	90
ZnO	Chemical	Nanoneedles	200	200	89	41	125	91
CuO–ZnO	Chemical	Flakes	200	5	8	13	5	46
ZnO	Chemical bath deposition	Nanotubes	200	1	20	1	30	Present work
				5	84	2.85	59	

materials demonstrates that ZnO-based sensors are capable of detecting NO_2 gas, as shown in Table 1.

ZnO-based gas sensors have shown to have rapid recovery/response rates, making them ideal for real-time detection of changes in NO_2 concentration.[42] This feature is particularly important for ensuring that appropriate measures are taken to reduce exposure to NO_2 and prevent potential health hazards. ZnO-based sensors can be utilized not only in industrial and outdoor air pollution monitoring, but also in applications such as indoor air quality monitoring, automotive emission control, and environmental monitoring.[43,44] With the continuous advancements in ZnO-based gas sensing technology, the development of even more efficient and reliable NO_2 sensors is expected. For instance, Patil et al.[45] reported a hierarchical ZnO nanostructure sensor using a catalyst-free thermal evaporation method and its recovery and response times for 1 ppm NO_2 were 180 and 48 seconds, respectively, at 200 °C. Chen et al.[46] reported CuO–ZnO nanocomposites synthesized using a chemical method. The gas response to 5 ppm NO_2 was 8% at 250 °C, with response and recovery times of 5 and 13 seconds. Patil et al.[47] reported ZnO nanorods for gas sensing applications using a hydrothermal route and found that the response/recovery times for 10 ppm NO_2 were 70 and 30 seconds at 200 °C. Based on the results mentioned above, it appears that the NO_2 gas sensors reported in the study may meet some of the desired criteria but not all of them. Ideally, a satisfactory sensor should exhibit fast response, have high selectivity, and demonstrate short response/recovery times. Furthermore, gas sensing selectivity can be enhanced by incorporating specific receptor materials that selectively interact with target gases.[48] Additionally, tailoring the sensor's surface properties and optimizing its operating conditions further contribute to its heightened selectivity in gas detection.[48,49]

Gas sensing properties are influenced not only by the chemical composition, but also by the morphology of the sensing material.[50] To date, various ZnO nanostructures, including one-dimensional (1D),[51,52] two-dimensional (2D),[53] and three-dimensional (3D)[54] structures, have been successfully synthesized for gas sensing applications. Among them, 1D nanostructures, especially nanotubes, have received a lot of interest due to their rapid gas diffusion, which significantly improves their gas sensing performance.[55,56] In contrast, ZnO nanotubes have emerged as promising candidates for gas sensing applications due to their unique structural and chemical properties.[55,57] The scope of ZnO

nanotubes in gas sensing lies in their high surface-to-volume ratio and large specific surface area, providing ample sites for gas molecules to interact, leading to enhanced sensitivity.[55] Additionally, their tubular morphology facilitates efficient charge transport and rapid response to changes in the gas environment. However, the limitations include challenges in reproducibility and scalability of the synthesis methods, which may hinder large-scale production.[58] Advantages of ZnO nanotubes include their intrinsic semiconducting nature, making them suitable for detecting a variety of gases.[59] Nevertheless, these sensors may suffer from selectivity issues, as they can be sensitive to multiple gases simultaneously.[58] Compared to other oxide materials, ZnO nanotubes exhibit improved sensitivity and response time, owing to their unique nanostructure.[55,57,58] The tubular geometry provides more active sites for gas adsorption, enhancing the overall performance. Moreover, ZnO nanotubes can outperform 2D materials in certain aspects due to their three-dimensional structure, offering a larger surface area for gas interaction.[59] This structural advantage contributes to a higher sensitivity and a lower detection limit, making ZnO nanotubes a preferable choice for gas sensing applications when compared to some conventional oxides and 2D materials.

In this investigation, we synthesized 1D ZnO nanotubes using a combination of chemical bath deposition (CBD) and thermal methods. The resulting ZnO nanotubes exhibited excellent gas sensitivity and an ultrafast response to NO_2 gas, especially at 200 °C working temperature. Models of ZnO nanotubes were proposed to explain the mechanism behind their gas sensitivity. Our findings demonstrate that ZnO nanotube sensors showed a high sensitivity of 84% towards 5 ppm NO_2 gas and 20% towards 1 ppm NO_2 gas, with ultrafast response times of 1 to 1.21 seconds for detecting both 1 and 5 ppm NO_2 gas.
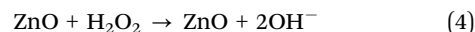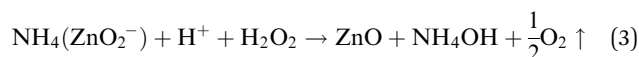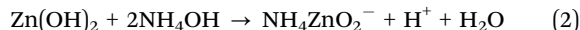
2. Experimental section
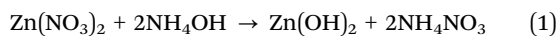
2.1. Precursors

The ZnO nanostructured films were synthesized on pre-cleaned glass substrates using 99.99% zinc nitrate hexahydrate [Zn $(NO_3)_2 \cdot 6H_2O$] (AR grade) as the precursor. The pH of the solution was adjusted by adding ammonia (NH_3) (SD fine chemicals) and hydrogen peroxide (H_2O_2) (Thomas Baker) was used as the oxidising agent.

2.2. Preparation of ZnO nanostructures

Fig. 1 depicts a schematic representation of the fabrication process of ZnO nanostructures using the CBD method. To prepare the reaction mixture, 2.97 g of Zn $(NO_3)_2 \cdot 6H_2O$ was dissolved in 50 ml of double distilled water at room temperature. Subsequently, NH_3 solution was added dropwise to adjust the pH to 12, and 2–3 ml of H_2O_2 was added to the solution, which was stirred for 20 minutes. The resulting mixture was transferred to a 100 ml cleaned beaker, where cleaned glass substrates were inserted vertically using a hanging system. The beaker was then placed in another large glass vessel containing paraffin oil, and the entire setup was placed on a magnetic stirrer with a temperature-controlled hot plate at 100 rpm. Sample deposition was carried out at an operating temperature of 70 °C for a duration of 3 hours, followed by 24 hours of drying at room temperature. The produced films were then calcined for 1 hour in air at 100, 200, 300, 400, 500, and 600 °C to obtain the zinc oxide products, indicated as ZnO-100, ZnO-200, ZnO-300, ZnO-400, ZnO-500, and ZnO-600. The calcination temperature can affect the crystal structure, surface area and morphology of ZnO nanostructures, which can influence their sensing properties.

During the CBD method, the cationic solution (containing metal ions) and the anionic solution (containing a source of anions such as hydroxide or nitrate) are mixed together. Ammonia (NH_3) is often used as a complexing agent to form metal–ammonia complexes, which are more stable and soluble than metal ions. Ammonia also acts as an anionic precursor, providing hydroxide ions (OH^-) through its reaction with water. These OH^- ions then react with metal ions to form metal hydroxide precursors, which can be further converted to metal oxide nanostructures through thermal treatment. The chemical reaction of ZnO nanostructures can be shown by eqn (1)–(4):

$$Zn(NO_3)_2 + 2NH_4OH \rightarrow Zn(OH)_2 + 2NH_4NO_3 \quad (1)$$

$$Zn(OH)_2 + 2NH_4OH \rightarrow NH_4ZnO_2^- + H^+ + H_2O \quad (2)$$

$$NH_4(ZnO_2^-) + H^+ + H_2O_2 \rightarrow ZnO + NH_4OH + \frac{1}{2}O_2 \uparrow \quad (3)$$

$$ZnO + H_2O_2 \rightarrow ZnO + 2OH^- \quad (4)$$

At lower temperatures, an excess portion of the Zn melted and approached the surface, leading to increased crystal growth and the formation of nanoparticles. As the calcination temperature increased to 500 °C, crystal growth became even more pronounced, and Zn dissipation was more efficient, resulting in the creation of a greater number of nanotubes. However, at higher calcination temperatures (600 °C), the nanotubes became broken due to the high temperature. These results suggest that careful control of calcination temperature can be used to tailor the microstructure of ZnO nanostructures for sensor devices.

2.3. Characterization techniques

The characteristics of the ZnO nanostructures have been examined using X-ray diffraction analysis (XRD, Rigaku, Ultima IV, Cu Kα/40 kV/40 mA), field emission scanning electron microscopy (FESEM, FEI Nova Nano SEM 450), and X-ray photoelectron spectroscopy (XPS, VG Multilab 2000, Thermo Scientific). The vibrational modes of the materials were analyzed using a Raman spectrometer (WITec-Alpha 300) with a laser wavelength of 532 nm. The specific surface area and pore size distribution of the materials were determined by performing BET analysis using NOVA and Quantachrome instruments.

2.4. Gas sensing test

Gas sensing tests were performed on ZnO nanostructures in a specialized 250cc gas sensor apparatus, and the ZnO nanostructure sensor's response to different gases was measured over a range of 100–300 °C. The target gases (H_2S, SO_2, ethanol, and NO_2)
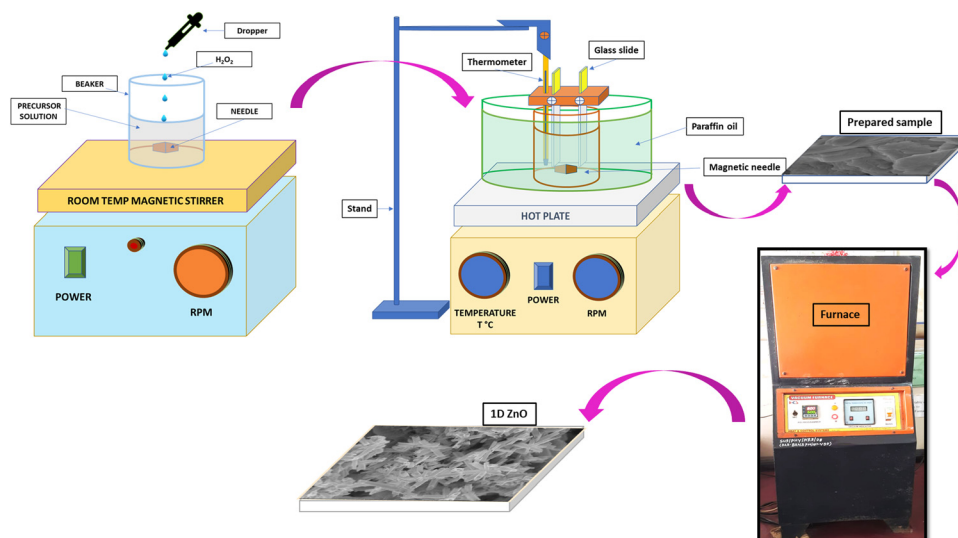

Fig. 1 Schematic representation of the various stages in the fabrication of 1D ZnO nanotubes using CBD.

© 2024 The Author(s). Published by the Royal Society of Chemistry

were sourced from certified cylinders with a purity level of 99%. The gas sensing data were collected using a Keithley-6514 programmable electrometer.[60] To find the optimum operating temperature, the sensitivity of a ZnO nanostructure sensor to 1 ppm and 5 ppm NO_2 was evaluated at various operating temperatures. Additionally, the sensor response/recovery properties were assessed by varying the concentrations of gas. The response (S%) was calculated using eqn (5):[32,33]

$$\text{Response, } S\ (\%) = \frac{R_g - R_a}{R_a} \times 100 \qquad (5)$$

where R_g and R_a represent the sensor resistance when exposed to the gas and air.

3. Results and discussion

3.1. Characterization of synthesized ZnO nanostructures

XRD is a widely used analytical technique that can be used to determine the crystalline structure. Fig. 2 shows the XRD patterns of ZnO-100, ZnO-200, ZnO-300, ZnO-400, ZnO-500, and ZnO-600 nanostructures, which reveal that all the samples have the same hexagonal crystalline structure with the space group $P63mc$ and lattice constants of $a = b = 0.32490$ nm and $c = 0.52040$ nm (ICSD 57450) (Fig. 2(a)). A pure phase with hexagonal crystal structure has formed, according to the Rietveld refinement study of the XRD pattern of ZnO-500, as illustrated

in Fig. 2(b). The lattice parameters were calculated using the Full-Prof suite software. Fig. 2(c) shows the schematic unit cell crystal structure obtained from output refinement data. The VESTA software package was used to visualize the crystal structure. The XRD analysis also provided information on the dislocation density (δ), stacking fault (SF), and micro-strain (ε), as indicated in Table S1 (ESI†).

$$\varepsilon = \frac{\beta \cos \theta}{4} \qquad (6)$$

$$\delta = \frac{1}{D^2} \qquad (7)$$

$$\text{SF} = \frac{2\pi^2}{45(3 \tan \theta)^{1/2}} \beta \qquad (8)$$

The ZnO nanostructures were found to be highly sensitive to calcination temperature, as evidenced by changes in microstrain, dislocation density and stacking fault.

Raman spectroscopy is indeed a powerful technique for identifying and characterizing vibrational modes in molecules. The ZnO-500 nanotubes exhibit four Raman-active modes: E_1 longitudinal optical (LO), E_2 (high), E_2 (low), and A_1 (TO) modes, as shown in Fig. 2(d). The E_1 longitudinal optical (LO) mode, which involves the displacement of Zn and O atoms in
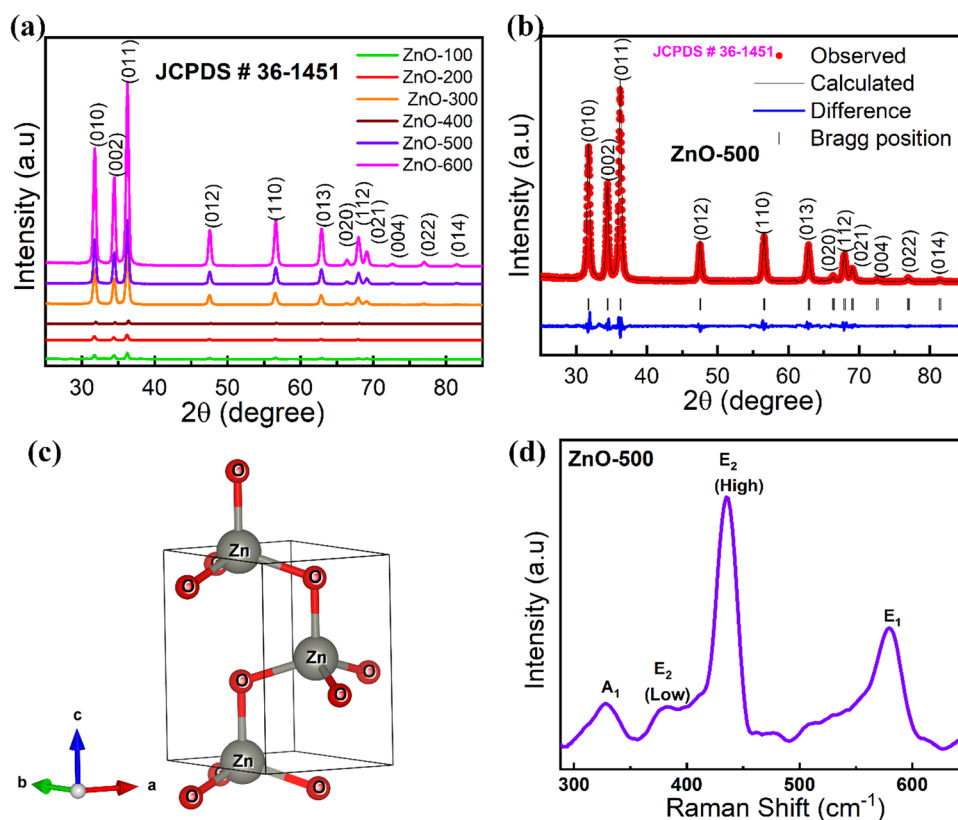

Fig. 2 Crystal structure determination. (a) XRD spectra of ZnO nanostructures produced on a glass substrate: ZnO-100, ZnO-200, ZnO-300, ZnO-400, ZnO-500 and ZnO-600 nanostructures. (b) Rietveld-refined XRD pattern of ZnO-500 nanostructures. (c) The crystal structures of ZnO-500 were determined by fitting data and visualized using the VESTA software. (d) Raman spectra of ZnO-500 nanostructures.

opposite directions along the *c*-axis, occurs at ~ 578 cm^{-1}.[43] The E$_2$ (high) mode, also known as the A$_1$ (longitudinal) mode or the Raman active mode, occurs at ~ 441 cm^{-1} and involves the in-plane vibration of O atoms. The E$_2$ (low) mode occurs at ~ 379 cm^{-1} and involves the out-of-plane vibration of Zn atoms; this mode is also known as the E$_1$ (transverse) mode or the Raman inactive mode. Finally, the A$_1$ mode occurs at ~ 332 cm^{-1} and involves transverse optical vibration of the oxygen atoms along the *c*-axis. This mode is also known as the E mode or the R_3 mode.

FESEM characterization was utilized to analyze the surface morphology of all ZnO nanostructure samples. ZnO-100 displayed a flake-like, porous structure (Fig. 3(a)), which is consistent with previous reports.[61,62] Fig. 3(b) and (c) show that the porous morphological structure becomes more prominent in the ZnO-200 and ZnO-300 nanostructures. The FE-SEM image of ZnO-400 in Fig. 3(d) shows the transformation of the porous structure into nanoparticles, which have dimensions ranging from 55.8 to 45.0 nm. Furthermore, the nanotube-like structure of ZnO-500 observed in Fig. 3(e) has a unique morphology with a nanotube length of approximately 400–700 nm, a diameter of 150 nm, and walls that are approximately 46 nm thick. The high aspect ratio of these structures has the potential to provide a large surface area, which could be useful for gas sensing applications. The rough and porous surface of the ZnO nanotubes observed at high magnification (as shown in the inset of Fig. 3(e)) can increase the surface area of the nanotubes. This enhanced surface area can create additional sites for gas adsorption and reaction, which can ultimately lead to improved sensitivity in gas sensing. The porous structure can also allow for better gas diffusion and access to the interior of the nanotubes, leading to more efficient gas sensing performance. However, higher calcination temperatures of ZnO-600 lead to the breakdown of these nanotubes, as shown in Fig. 3(f). The diameter of the broken holes ranges from 505 to 605 nm, which can restrict their suitability for gas sensing applications. Fig. 3(g) presents a histogram of 1D ZnO-500 nanotube size distribution, with an average nanotube length of 500–700 nm. Additionally, Fig. 3(h) shows EDS mapping of the nanotubes, confirming the successful synthesis of ZnO.

EDS analysis was performed to obtain elemental mapping of Zn and O in ZnO-100, ZnO-200, ZnO-300, ZnO-400, and ZnO-600 nanostructures, as depicted in Fig. S1 (ESI†). The results demonstrate that Zn and O are the primary elements present in the prepared samples, indicating the formation of ZnO nanostructures. Moreover, the chemical composition and purity of ZnO-100, ZnO-200, ZnO-300, ZnO-400, ZnO-500, and ZnO-600 nanostructures were analyzed using EDS spectra, which are displayed in Fig. 4(a)–(f). The inset tables in Fig. 4(a)–(f) provide the atomic and weight % and intensities of Zn and O in each sample. The data suggest that the calcination process caused some variation in the atomic and weight percentages, which could be attributed to heat agitation in the prepared samples.

The BET surface area measurement is a widely used method for determining the specific surface area of a material. It relies on analyzing the adsorption isotherm of a gas onto a solid
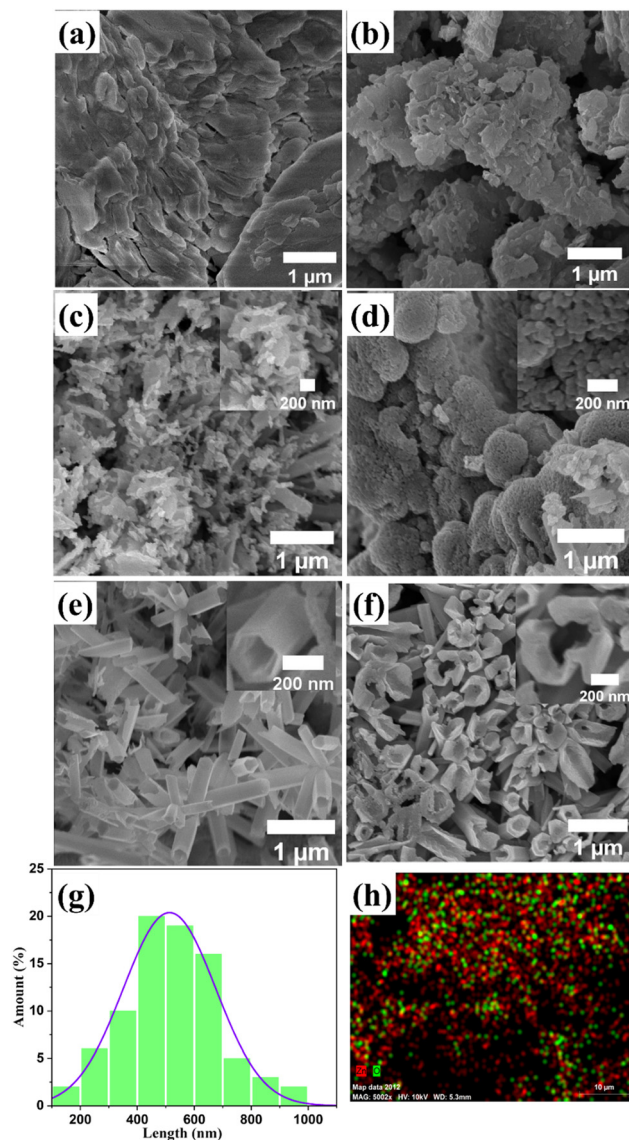

Fig. 3 FESEM images of ZnO nanostructures. (a) ZnO-100 shows a porous and flake-type structure, (b) ZnO-200 shows a porous structure, (c) ZnO-300 shows a porous structure with a high porosity, (d) ZnO-400 shows nanoparticles, (e) ZnO-500 shows nanotubes, (f) ZnO-600 shows broken nano-holes. (g) Histogram plot showing the length distribution of ZnO-500 nanotubes and (h) EDS mapping of ZnO-500 nanotubes.

surface, with the amount of gas adsorbed being proportional to the surface area of the material. Fig. S2 (ESI†) depicts the surface areas and nitrogen physical adsorption–desorption isotherms of different ZnO nanostructures. Surface area is a critical structural property greatly influenced by morphology. The BET surface areas of ZnO-300 (porous structures), ZnO-400 (nanoparticles), ZnO-500 (nanotubes), and ZnO-600 (broken nanotubes) are 30.4527, 40.8447, 56.9546, and 50.5161 m^2 g^{-1}, respectively. These BET findings show that nanotubes have a greater surface area than porous structures, nanoparticles, and broken nanotubes. This suggests that the cylindrical shape of the nanotube structure is responsible for its larger surface area when compared to other structures. Nanotubes are cylindrical
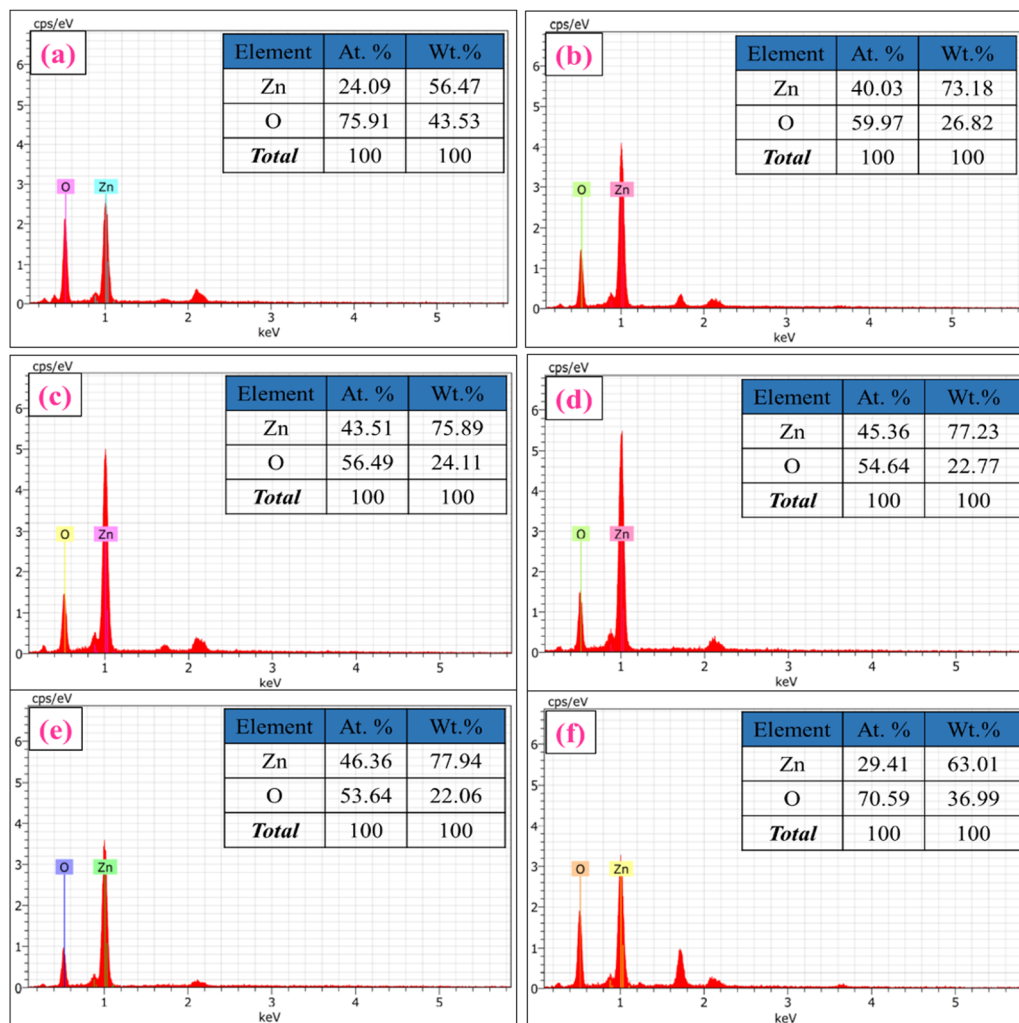
Fig. 4 EDS spectra and elemental composition of ZnO nanostructures. (a) ZnO-100, (b) ZnO-200, (c) ZnO-300, (d) ZnO-400, (e) ZnO-500, and (f) ZnO-600.

structures that provide a very large surface area per unit mass. The walls of the nanotubes are also very thin, typically only 46 nm in thickness, which means that a significant fraction of the atoms in the material are located on the surface. This leads to a very high surface area and makes nanotubes attractive for gas sensing. On the other hand, the lower surface area of ZnO-300 porous structures can be attributed to their irregular and disordered morphology, which leads to a lower surface area per unit mass. The same is true for ZnO-400 nanoparticles, which have a relatively low surface area due to their small size and spherical shape. ZnO-400 (nanoparticles) has a higher surface area compared to ZnO-300 because the nanoparticles have a smaller size and higher surface-to-volume ratio, resulting in a larger surface area per unit mass. ZnO-600 broken nanotubes, although they have a similar morphology to nanotubes, have a lower surface area compared to ZnO-500, possibly due to structural defects that may have occurred during the breakdown process. The breakdown of the nanotube structure reduces the overall surface area of the ZnO-500 sample.

XPS was employed to clarify the compositions and electronic states of ZnO nanostructure samples. In the ESI,† Fig. S3(a)–(f) shows a wide region survey spectrum of ZnO nanostructures, which indicates the presence of oxygen (O), zinc (Zn), and carbon (C) elements in the ZnO-100 to ZnO-600 nanostructures. The peak observed at around 537–528 eV indicates the presence of oxidized metal ions O–Zn in ZnO. In Fig. 5(a), high-resolution XPS spectra of ZnO-100 nanostructures show the absence of elemental Zn in ZnO nanostructures, as evidenced by a shift in the binding energy (BE) over 1021 eV. The peak at 1021.3 eV is associated with Zn $2p_{3/2}$ species in stoichiometric ZnO.[63] The additional peak at 1025 eV corresponds to groups of –OH connected to Zn ions on the nanostructures' surfaces or Zn-deficient areas.[63,64] The Zn $2p_{1/2}$ XPS spectra generated two satellites at 1045.1 and 1050.1 eV, corresponding to Zn $2p_{1/2}$ in the ZnO matrix and the –OH impurities bound to Zn ions.[63] As shown in Fig. 5(b), the ZnO-500 nanostructures displayed two peaks in the Zn 2p spectrum at around 1043.69 and 1020.68 eV, respectively. These peaks corresponded to Zn $2p_{1/2}$ and Zn $2p_{3/2}$.[65,66] The XPS data suggest that a low calcination temperature of 100 °C (ZnO-100 porous nanostructures) shows groups of –OH connected to Zn ions on the nanostructures' surfaces, while a higher calcination temperature of 500 °C (ZnO-500 nanotubes) exhibits pure ZnO nanostructures.
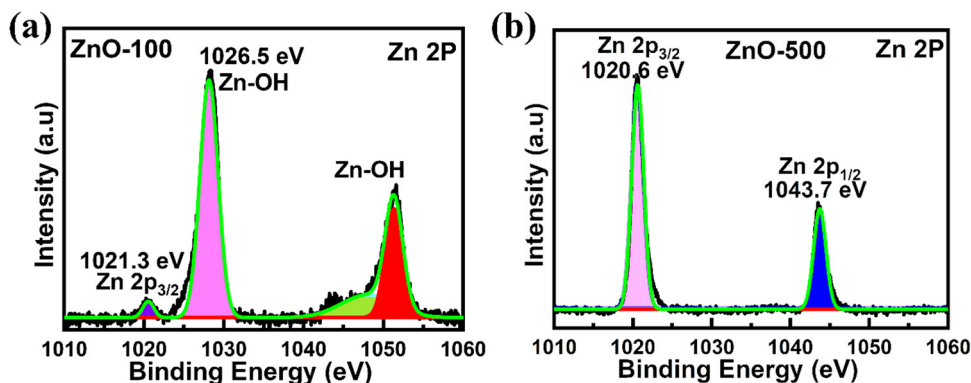
Fig. 5 XPS spectra of the Zn 2p peak of ZnO nanostructures of (a) ZnO-100 and (b) ZnO-500 samples.

3.2. Gas sensing studies

3.2.1. Working temperature effect. Determining the optimal working temperature is crucial for the performance of gas sensors. The sensor response values are typically influenced by the sensing temperature due to temperature-dependent gas adsorption and diffusion phenomena.[67,68] In this study, tests were conducted to determine the optimal working temperature of the ZnO-500 sensor. The sensor response values were measured as a function of the working temperature, as depicted in Fig. 6(a) and (b). It was observed that the sensor responded to NO_2 gas concentrations of 1 ppm and 5 ppm at all sensing temperatures; nevertheless, its response was noticeably impacted by the sensing temperature. The lower temperatures may not offer enough energy to achieve effective NO_2 gas adsorption, which can result in higher desorption rates relative to adsorption rates at higher temperatures. According to the test results, it was observed that the gas sensor made using ZnO-500 nanotubes demonstrated the best responses of 20% and 84% at 200 °C for 1 and 5 ppm concentrations. However, the response rates decreased at 250 °C and 300 °C. The efficiency of gas sensing can be significantly impacted by the sensing temperature as the processes of desorption, diffusion, and adsorption are all dependent on
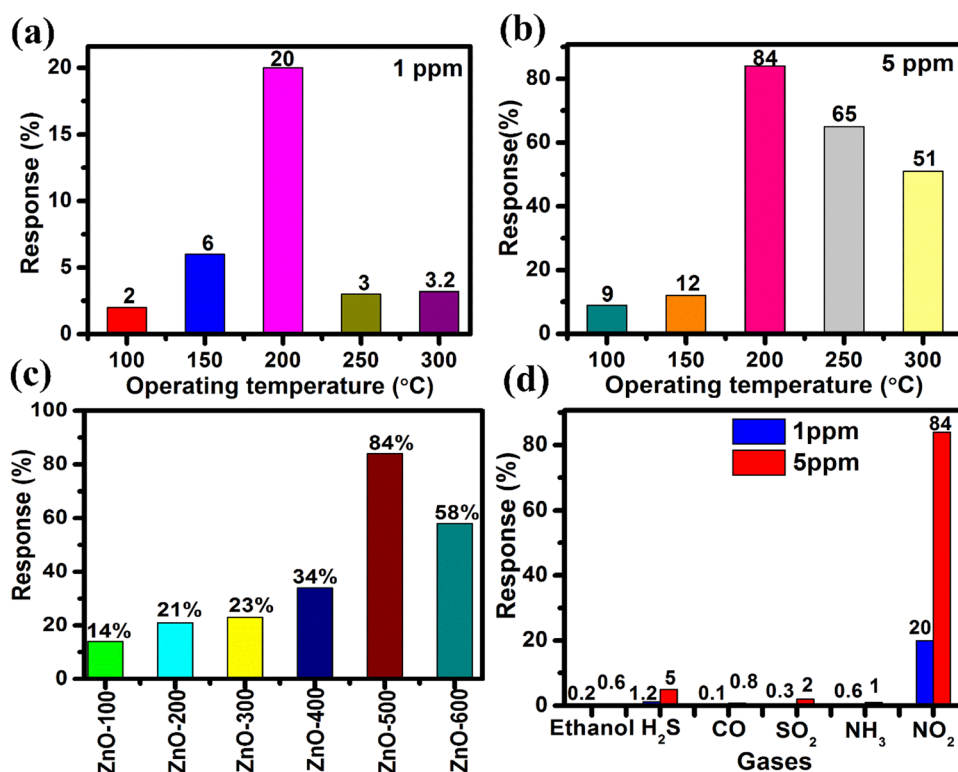

Fig. 6 (a) and (b) The response of the ZnO-500 nanotube sensor measured at different operating temperatures for 1 ppm and 5 ppm NO_2 gas. (c) The selectivity responses of ZnO-100, ZnO-200, ZnO-300, ZnO-400, ZnO-500 and ZnO-600 nanostructures sensors to various gases measured at 200 °C at a gas concentration of 5 ppm NO_2. (d) The response of the ZnO-500 nanotube sensor to various gases measured at different operating temperatures for 1 ppm and 5 ppm gas concentrations.

© 2024 The Author(s). Published by the Royal Society of Chemistry

temperature. When the temperature falls below the optimal range, sensor's responsiveness decreases due to deactivation of diffusion and desorption processes. Conversely, when the temperature exceeds the optimal range, the sensing efficiency is compromised because adsorption becomes inefficient, and desorption takes place too rapidly.[69] Therefore, the gas sensor's response decreases at 300 °C, which is above the optimal sensing temperature for NO_2 gas sensing. In the case of the NO_2 gas sensors discussed, it was observed that 200 °C is the optimal temperature for reliable and accurate gas detection.

3.2.2. Selectivity study. The performance of a sensor depends significantly on its selectivity, which refers to the sensor's capacity to detect the target gas specifically and exclude interference from other gases. In the case of the ZnO nanostructure sensor, the selectivity was tested using a custom-fabricated gas detecting unit for NO_2 gas at 5 ppm at 200 °C. The ZnO-500 sensor demonstrated an exceptional response of 84% for 5 ppm concentration of NO_2, while other sensors displayed notably lower responses. The responses were 14% for ZnO-100, 21% for ZnO-200, 34% for ZnO-300, 50% for ZnO-400, and 58% for ZnO-600, as illustrated in Fig. 6(c). The ZnO-500 nanotube sensor responds to NO_2 more strongly than the ZnO-100, ZnO-200, ZnO-300, ZnO-400, and ZnO-600 sensors. This difference can be attributed to the particle sizes and the gradual agglomeration of particles at low treatment temperatures. As a result, the reduced specific surface areas negatively impact the adsorption of NO_2 molecules on the sensing materials' surfaces, leading to a decline in their responses. In addition, 1D ZnO nanotubes have a very high aspect ratio, which

means that their length (~700 nm) is much greater than their diameter (~150 nm). The high aspect ratio of ZnO 1D nanotubes provides them with a high surface area-to-volume ratio, which allows them to interact more effectively with the target molecules. When exposed to a gas, the molecules adsorb onto the nanotube surface, causing a change in its electrical properties. This change can then be detected and used to determine the presence and concentration of the target molecules. The large surface area of ZnO 1D nanotubes is also beneficial because it enhances their sensitivity and selectivity. The increased surface area provides more opportunities for the target molecules to interact with the nanotubes, resulting in a greater sensor response. Moreover, the high aspect ratio of the nanotubes provides better control over the orientation and positioning of the target molecules, potentially leading to improved selectivity of the sensor.[70]

Furthermore, the selectivity of the ZnO-500 nanotube sensor was tested using a custom-fabricated gas detecting unit for various gases including ethanol, H_2S, CO, NH_3, SO_2 and NO_2 at 5 ppm and 1 ppm at 200 °C, as depicted in Fig. 6(d). The results of the selectivity analysis demonstrate that the prepared ZnO-500 nanotube sensor is more responsive to NO_2 gas compared to other gases such as ethanol, H_2S, CO, NH_3 and SO_2.

3.2.3. Response and recovery time values. Fig. 7(a) illustrates the results of an investigation into the gas response of a 1D ZnO nanotube sensor for NO_2 gas concentrations between 1 and 5 ppm and results show that the sensor response increases with an increase in gas concentration as illustrated in Fig. 7(a). Fig. 7(b) shows the sensor's 20% response at an NO_2
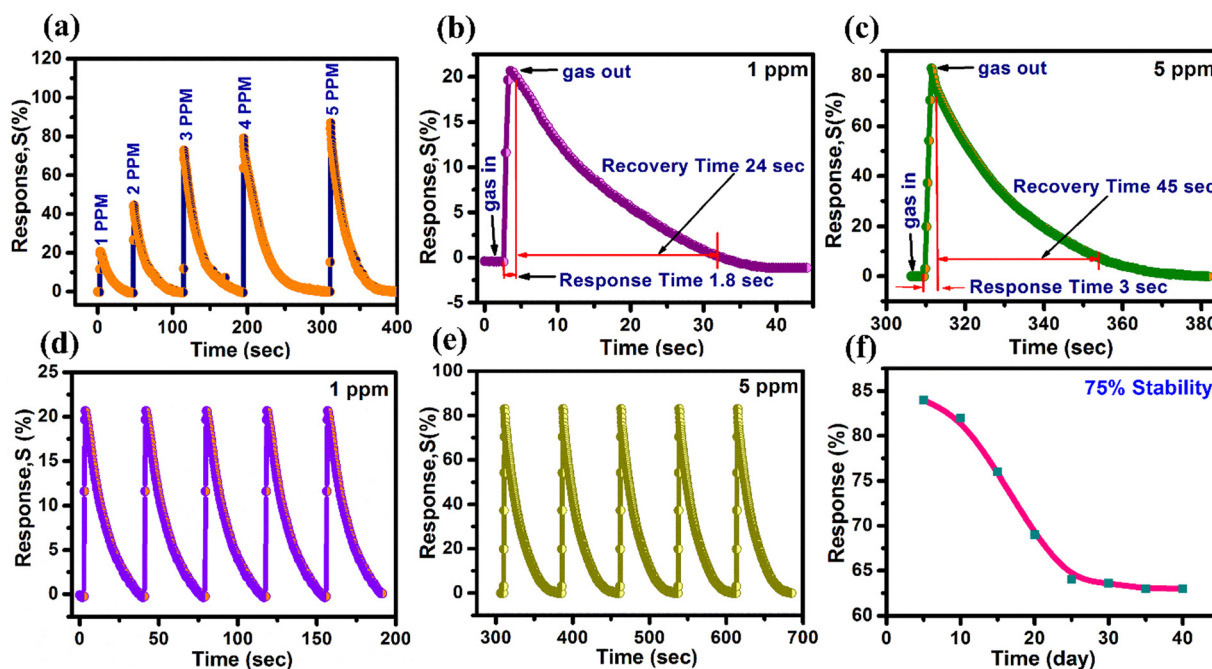

Fig. 7 (a) The response–recovery curves of ZnO nanostructures for NO_2 detection at various concentrations at an operating temperature of 200 °C. (b) The response transient of ZnO-500 nanotubes for 1 ppm NO_2 was recorded at a working temperature of 200 °C. (c) The response transient of ZnO-500 nanotubes for 5 ppm NO_2 was recorded at 200 °C. (d) and (e) The reproducibility evaluated for 1 ppm and 5 ppm NO_2 gas. (f) A long-term stability test conducted with 5 ppm NO_2 gas.
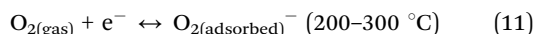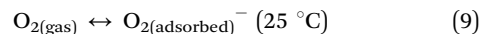
concentration of 1 ppm, with a response time of 1 second and 30 seconds for recovery. At an NO_2 concentration of 5 ppm, the 1D ZnO nanotube sensor exhibited a maximum response of 84%, with a response time of 2.85 seconds and a recovery time of 59 seconds as depicted in Fig. 7(c). Table 2 summarizes the sensor response, response time, and recovery time of the 1D ZnO nanotube sensor at different concentrations of NO_2. The response and recovery times vary with different concentrations of NO_2, as shown in Fig. S4 (ESI†). Compared to other NO_2 sensors documented in Table 1, the 1D ZnO nanotube sensor exhibits a faster response time and a shorter recovery period. In contrast, the ZnO-500 nanotube sample has shown fast response and recovery times for detecting low levels of NO_2 gas, making it a promising material for practical applications such as air quality monitoring, industrial emission control, and automotive exhaust systems.[71–73]

3.2.4. Reproducibility and stability studies. Reproducibility refers to the ability of a sensor to produce consistent and reliable results when tested multiple times under the same conditions. In practical applications, the reliability and effectiveness of a sensor depend significantly on its reproducibility and stability. These factors are crucial for ensuring that the sensor can produce consistent and accurate results over time. The reproducibility of the 1D ZnO-500 nanotube sensor was assessed by measuring its response to 1 and 5 ppm NO_2 at 200 °C for five testing cycles. The sensor showed excellent reproducibility, maintaining its initial response after each cycle, as shown in Fig. 7(d) and (e). Furthermore, stability of the sensor was determined by measuring its response to 5 ppm NO_2 concentration every five days for a period of 40 days, as depicted in Fig. 7(f). The sensor's response remained stable, changing by less than 25% even after 40 days, indicating that the sensor was highly stable. The 1D ZnO-500 nanotube sensor has demonstrated outstanding reproducibility and stability in detecting NO_2 gas, suggesting that this sensor has high potential for practical applications as a reliable and long-lasting device for detecting nitrogen dioxide gas.

3.2.5. Gas sensing mechanism. According to electron depletion theory, when NO_2 gas comes into contact with the surface of ZnO nanotubes, it reacts with the surface oxygen ions to form nitrate ions and oxygen vacancies.[74,75] This reaction causes the depletion of electrons in the ZnO nanotubes, resulting in a decrease in the electrical conductivity of the nanotubes. The magnitude of the decrease in conductivity is proportional to the concentration of NO_2 gas in the environment. Therefore, the change in the electrical conductivity of ZnO nanotubes can

be used to detect the concentration of NO_2 gas in the environment. The sensing mechanism of ZnO nanotubes to detect NO_2 is depicted in Fig. 8. When the ZnO nanotube gas sensor comes into contact with the air, O_2 molecules remove electrons from the surface of the sensor, resulting in the production of oxygen species (O^{2-}, O_2^- and O^-) and the formation of a layer on the surface of ZnO depleted of electrons.[76,77]

$$O_{2(gas)} \leftrightarrow O_{2(adsorbed)}^- \ (25 \ °C) \tag{9}$$

$$O_{2(gas)} + e^- \leftrightarrow 2O_{2(adsorbed)}^- \ (25\text{--}200 \ °C) \tag{10}$$

$$O_{2(gas)} + e^- \leftrightarrow O_{2(adsorbed)}^- \ (200\text{--}300 \ °C) \tag{11}$$

As the experiments are conducted at 200 °C, the production of O^{-2} will occur (according to eqn (10)). Furthermore, when exposed to NO_2 gas, the NO_2 molecules adsorbed onto the surface of the ZnO nanotubes will interact with the oxygen species that are also adsorbed onto the surface. This results in the NO_2 molecules capturing more electrons from the conduction band of ZnO, causing the depletion layer to widen and the resistance of the ZnO sensor to increase.[78] The overall reaction can be presented as follows:

$$NO_{2(gas)} + e^- \rightarrow NO_{2(ads)}^- \tag{12}$$
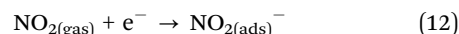
NO_2 molecules capture electrons (e^-) and are converted into NO_2^- ions.

$$NO_{2(gas)}^- + O_{2(ads)}^- + 2e^- \rightarrow NO_{2(ads)}^- + 2O_{(ads)}^- \tag{13}$$
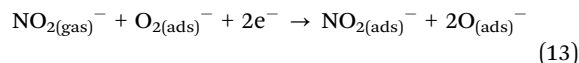
NO_2^- ions react with O_2^- ions and two electrons to produce NO_2^- and two O_2^- ions.

In the absence of NO_2 gas, the resistance of the ZnO nanotubes returns to its original value when exposed to air. This is because the adsorbed NO_2 gas molecules gradually desorb from the nanotube surface and return to the gas phase. When the NO_2 gas molecules desorb from the surface of the nanotubes, the electron density and hence the conductivity of the nanotubes return to their original values. This is because the existence of NO_2 gas alters the electron density of the ZnO nanotubes, leading to a change in their electrical conductivity. In contrast, in the gas adsorption process on ZnO nanotubes, NO_2 gas molecules interact with the surface, capturing electrons

Table 2 The sensing responses of a 1D ZnO-500 sensor were investigated for 1–5 ppm NO_2 gas at 200 °C operating temperature

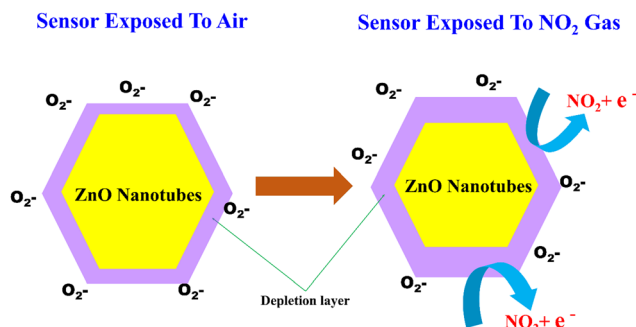| NO_2 concentration (ppm)	Response (%)	Response time (s)	Recovery time (s)
1	20	1	30
2	44	1.21	41
3	74	1.8	47
4	79	2.6	56
5	84	2.85	59

Fig. 8 Schematic representation of the gas sensing mechanism of 1D ZnO nanotubes in air and in gas.

and leading to the widening of the depletion layer. This interaction increases the resistance of the nanotubes. Concurrently, oxygen species present on the ZnO surface facilitate this adsorption mechanism. Conversely, during the desorption process, the ZnO nanotubes are heated, prompting the release of the previously adsorbed NO_2 molecules. This heating-driven desorption effectively restores the original configuration of the ZnO sensor, preparing it for subsequent detection events.

The high surface area to volume ratio of ZnO nanotubes provides an increased number of active sites for gas adsorption, which enhances the gas sensing properties of ZnO nanotubes. The unique tubular structure also provides a higher degree of freedom for gas molecules to interact with the ZnO nanotubes, leading to a more efficient gas sensing response. Additionally, the tubular structure of ZnO nanotubes can offer mechanical flexibility, which can help maintain the stability and durability of the gas sensing device during sensing operations. Overall, the tubular structure of ZnO nanotubes makes them promising candidates for gas sensing devices.

3.3. Impedance spectroscopy

Impedance measurements are a common method for studying the electrical properties of materials and gas sensing devices.[79–83] In the case of the ZnO nanotube sensor, impedance measurements were conducted to investigate the changes in electrical properties before and after exposure to NO_2 gas as illustrated in Fig. 9(a). The impedance graph shows a semi-circular curve that ranges from low (20 Hz) to high frequencies (10 MHz) when the imaginary component (Z'') is plotted *versus* the real component (Z'). This is a characteristic feature of a parallel resistor–capacitor (RC) circuit, as shown in Fig. 9(b). The impedance data were generated using an equivalent circuit model composed of three parallel RC networks and one series resistor. The circuit model parameters consist of R_e and C_e, representing electrode contact resistance and capacitance; R_o, R_b and R_{gb} represent initial, bulk boundary and grain resistances; and C_{gb} and C_b represent grain boundary and bulk capacitances.[60,79,80,84–88] Table 3 presents the simulated values of these parameters for both air and NO_2 environments. The results show that R_e, R_b, and R_{gb} increased

Table 3 Values of parameters of the equivalent circuit for fitting the impedance spectra of the 1D ZnO nanotube sensor measured in air and NO_2 ambient

Parameters	R_0 (KΩ)	R_e (MΩ)	R_{gb} (MΩ)	R_b (MΩ)	C_e (pF)	C_{gb} (pF)	C_b (pF)
In air	6.006	6.3153	7.8318	4.1111	17.10	21.68	20.22
In gas	6.006	14.8423	20.9534	15.7207	7.882	1.316	4.02

when the ZnO nanotube sensor was exposed to NO_2 gas, while C_e, C_b, and C_{gb} decreased. NO_2 gas adsorption on the surface of n-type ZnO nanotubes results in an increase in resistance.[89] The process of adsorbing these gas molecules can lead to the trapping of some free electrons within the conduction band. This reduces the number of available free electrons and increases the resistance of the material, making it harder for electric current to flow through the nanotubes. As a result, the electrical conductivity of the material is reduced, which can be measured as an increase in resistance. The electrical properties of n-type ZnO nanotubes undergo changes upon the adsorption of NO_2 gas molecules. Fig. 9(a) demonstrates that the agreement between the experimental data and the software simulation data indicates the accuracy of the equivalent circuit model used to simulate the impedance data. The model can be utilized to predict changes in the electrical properties of the ZnO nanotube sensor when exposed to NO_2 gas. It should be noted that the solid lines in the figure represent the experimental data, while the symbols represent the software simulation data.

The study investigates the gas sensing capabilities of 1D ZnO-500 nanotubes through several tests, such as selectivity response/recovery time and impedance spectroscopy, when exposed to NO_2 gas at concentrations of 1 and 5 ppm. The results show that the nanotubes exhibit gas responses of 20% at 1 ppm and 84% at 5 ppm when operated at a temperature of 200 °C. These sensitivity levels are higher than those of other materials such as ZnO nanosheets,[90] ZnO nanoneedles,[91] a bunch of ZnO nanowires,[45] and CuO–ZnO flakes.[46] These findings imply that 1D ZnO nanotubes have the potential to be employed as an NO_2 sensor device. In addition, 1D ZnO nanotubes have been shown to exhibit response and recovery times of 1/30 seconds and 2.85/59 seconds in the presence of
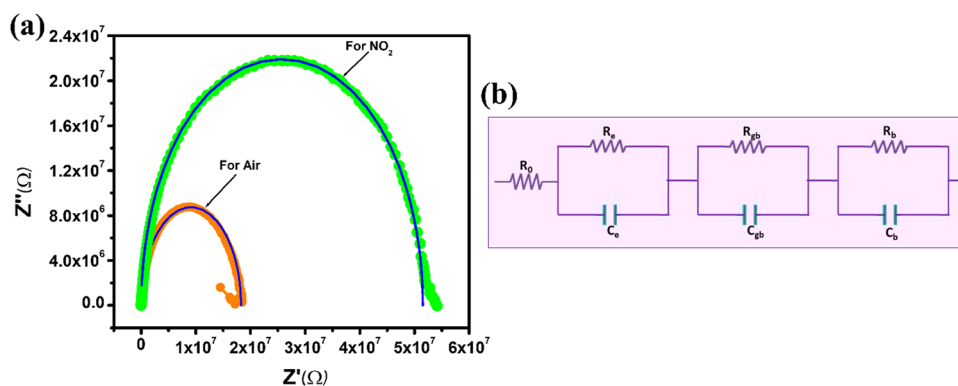

Fig. 9 (a) Nyquist impedance plot that shows the electrical behavior of ZnO-500 nanotubes when exposed to air and NO_2 gas at a concentration of 5 ppm and a temperature of 200 °C. (b) Impedance fitting circuit.

NO_2 concentrations of 1 ppm and 5 ppm. These times are faster than those of other materials, including macro-to-mesoporous ZnO,[92] ZnO nanowires,[93] ZnO spheres,[94] Pr doped ZnO nanospindles,[95] and BiOI–ZnO microballs.[96] Therefore, these results suggest that 1D ZnO nanotubes are a promising material for use in real-time monitoring applications, such as air quality monitoring systems, that require swift detection and response times to ensure public health and safety.[71–73,97]

4. Conclusion

ZnO nanotubes synthesized using chemical bath deposition and thermal methods show promising potential for NO_2 gas detection. The resultant 1D ZnO-500 nanotube sensor demonstrated outstanding sensitivity to NO_2 gas, operating at 200 °C with a response sensitivity of 84% for 5 ppm NO_2 and 20% for 1 ppm NO_2. The NO_2 detection limit of 1 ppm is considerably lower than the critical exposure limit of 20 ppm. The response and recovery times for 1 ppm NO_2 were 1 and 30 seconds, respectively, while for 5 ppm NO_2, the response and recovery times were 2.85 and 59 seconds, respectively. The sensor demonstrated outstanding stability, retaining 75% of its initial sensing performance over 40 days. Impedance spectroscopy results highlighted an increase in resistance due to the interaction of gases with adsorbed NO_2 gas molecules. The outstanding NO_2 gas-sensing ability may be due to the synergistic effect, inherent structural properties of 1D ZnO-500 nanotubes and surface-adsorbed oxygen species. The NO_2 sensor's detection limit of 5 ppm meets the requirements of various regulatory bodies, making it suitable as a potential sensor device in real-world environments for NO_2 gas detection.

Author contributions

Prasad Godse: investigation, writing the original manuscript and developing the methodology; Sujit A. Kadam: writing the original manuscript, conducting analysis, curating the data, and editing and reviewing the manuscript; T. M. Nimbalkar: editing and revising the manuscript; Y. M. Jadhav supervision; Yuan-Ron Ma: supervision; Yuvraj B Jadhao: analysis; and Professor V. B. Patil: investigation, providing necessary resources, editing and revising the manuscript, and writing original content. They also provided supervision throughout the project.

Data availability

Data will be provided upon request.

Conflicts of interest

There is no conflict of interest for the authors.

References

1 C. Chen, G. Xie, J. Dai, W. Li, Y. Cai, J. Li, Q. Zhang, H. Tai, Y. Jiang and Y. Su, Integrated core-shell structured smart textiles for active NO_2 concentration and pressure monitoring, *Nano Energy*, 2023, **116**, 108788.

2 H. Pan, G. Chen, Y. Chen, A. Di Carlo, M. A. Mayer, S. Shen, C. Chen, W. Li, S. Subramaniam, H. Huang, H. Tai, Y. Jiang, G. Xie, Y. Su and J. Chen, Biodegradable cotton fiber-based piezoresistive textiles for wearable biomonitoring, *Biosens. Bioelectron.*, 2023, **222**, 114999.

3 J. Li, G. Xie, J. Jiang, Y. Liu, C. Chen, W. Li, J. Huang, X. Luo, M. Xu, Q. Zhang, M. Yang and Y. Su, Enhancing photodegradation of Methyl Orange by coupling piezo-phototronic effect and localized surface plasmon resonance, *Nano Energy*, 2023, **108**, 108234.

4 Y. Su, Y. Liu, W. Li, X. Xiao, C. Chen, H. Lu, Z. Yuan, H. Tai, Y. Jiang, J. Zou, G. Xie and J. Chen, Sensing–transducing coupled piezoelectric textiles for self-powered humidity detection and wearable biomonitoring, *Mater. Horiz.*, 2023, **10**, 842–851.

5 L. Liu, Y. Wang, K. Guan, Y. Liu, Y. Li, F. Sun, X. Wang, C. Zhang, S. Feng and T. Zhang, Influence of oxygen vacancies on the performance of SnO_2 gas sensing by near-ambient pressure XPS studies, *Sens. Actuators, B*, 2023, **393**, 134252.

6 S. T. Navale, X. G. Gui, P. Cao, N. Joshi, F. J. Stadler, S. S. Kim and H. W. Kim, Morphology engineering of hierarchical spinal nickel-cobaltite nanostructures for enhanced ethanol detection, *Nano-Struct. Nano-Objects*, 2023, **34**, 100981.

7 A. Alagh, F. E. Annanouch, A. Sierra-Castillo, E. Haye, J.-F. Colomer and E. Llobet, Three-Dimensional Assemblies of Edge-Enriched WSe_2 Nanoflowers for Selectively Detecting Ammonia or Nitrogen Dioxide, *ACS Appl. Mater. Interfaces*, 2022, **14**, 54946–54960.

8 X. Wang, Y. Yong, W. Yang, A. Zhang, X. Xie, P. Zhu and Y. Kuang, Adsorption, Gas-Sensing, and Optical Properties of Molecules on a Diazine Monolayer: A First-Principles Study, *ACS Omega*, 2021, **6**, 11418–11426.

9 L. Arellano-García, S. Le Borgne and S. Revah, Simultaneous treatment of dimethyl disulfide and hydrogen sulfide in an alkaline biotrickling filter, *Chemosphere*, 2018, **191**, 809–816.

10 R. N. Dhanawade, N. S. Pawar, M. A. Chougule, G. M. Hingangavkar, T. M. Nimbalkar, G. T. Chavan, C.-W. Jeon and V. B. Patil, Influence of the Camphor Sulphonic Acid (CSA) Intercalation on the Micro-structural and Gas Sensing Properties of Polyaniline-CeO_2 Nanohybrid for NH_3 Gas Detection, *ChemistrySelect*, 2023, **8**, e202204750.

11 E. Martínez-Ahumada, M. L. Díaz-Ramírez, Md. J. Velásquez-Hernández, V. Jancik and I. A. Ibarra, Capture of toxic gases in MOFs: SO_2, H_2S, NH_3 and NO_x, *Chem. Sci.*, 2021, **12**, 6772–6799.

12 Y. Uesugi, H. Nagakawa and M. Nagata, Highly Efficient Photocatalytic Degradation of Hydrogen Sulfide in the Gas Phase Using Anatase/TiO_2(B) Nanotubes, *ACS Omega*, 2022, **7**, 11946–11955.

13 L. Yang, G. Zheng, Y. Cao, C. Meng, Y. Li, H. Ji, X. Chen, G. Niu, J. Yan, Y. Xue and H. Cheng, Moisture-resistant,

stretchable NO_x gas sensors based on laser-induced graphene for environmental monitoring and breath analysis, *Microsyst. Nanoeng.*, 2022, **8**, 78.

14 X. Geng, S. Li, L. Mawella-Vithanage, T. Ma, M. Kilani, B. Wang, L. Ma, C. C. Hewa-Rahinduwage, A. Shafikova, E. Nikolla, G. Mao, S. L. Brock, L. Zhang and L. Luo, Atomically dispersed Pb ionic sites in PbCdSe quantum dot gels enhance room-temperature NO_2 sensing, *Nat. Commun.*, 2021, **12**, 4895.

15 M. A. G. Demetillo, A. Navarro, K. K. Knowles, K. P. Fields, J. A. Geddes, C. R. Nowlan, S. J. Janz, L. M. Judd, J. Al-Saadi, K. Sun, B. C. McDonald, G. S. Diskin and S. E. Pusede, Observing Nitrogen Dioxide Air Pollution Inequality Using High-Spatial-Resolution Remote Sensing Measurements in Houston, Texas, *Environ. Sci. Technol.*, 2020, **54**, 9882–9895.

16 M. U. Ali, Y. Yu, B. Yousaf, M. A. M. Munir, S. Ullah, C. Zheng, X. Kuang and M. H. Wong, Health impacts of indoor air pollution from household solid fuel on children and women, *J. Hazard. Mater.*, 2021, **416**, 126127.

17 W. Huang, X. Zhuang, F. S. Melkonyan, B. Wang, L. Zeng, G. Wang, S. Han, M. J. Bedzyk, J. Yu, T. J. Marks and A. Facchetti, UV–Ozone Interfacial Modification in Organic Transistors for High-Sensitivity NO_2 Detection, *Adv. Mater.*, 2017, **29**, 1701706.

18 M. J. Cooper, R. V. Martin, M. S. Hammer, P. F. Levelt, P. Veefkind, L. N. Lamsal, N. A. Krotkov, J. R. Brook and C. A. McLinden, Global fine-scale changes in ambient NO_2 during COVID-19 lockdowns, *Nature*, 2022, **601**, 380–387.

19 A. Moumen, R. Konar, D. Zappa, E. Teblum, I. Perelshtein, R. Lavi, S. Ruthstein, G. D. Nessim and E. Comini, Robust Room-Temperature NO_2 Sensors from Exfoliated 2D Few-Layered CVD-Grown Bulk Tungsten Di-selenide ($2H$-WSe_2), *ACS Appl. Mater. Interfaces*, 2021, **13**, 4316–4329.

20 Z. Feng, H. Wang, Y. Zhang, D. Han, Y. Cheng, A. Jian and S. Sang, ZnO/GaN n-n heterojunction porous nanosheets for ppb-level NO_2 gas sensors, *Sens. Actuators, B*, 2023, **396**, 134629.

21 H. Chi, Z. Xu, X. Duan, J. Yang, F. Wang and Z. Li, High-Performance Colorimetric Room-Temperature NO_2 Sensing Using Spin-Coated Graphene/Polyelectrolyte Reflecting Film, *ACS Appl. Mater. Interfaces*, 2019, **11**, 32390–32397.

22 V. V. Ganbavle, S. I. Inamdar, G. L. Agawane, J. H. Kim and K. Y. Rajpure, Synthesis of fast response, highly sensitive and selective Ni:ZnO based NO_2 sensor, *Chem. Eng. J.*, 2016, **286**, 36–47.

23 J. Zeng, Y. Xu, J. Yu, X. Zhang, X. Zhang, H. Jin, Q. Jin, W. Shen, J. Zou, S. Deng and J. Jian, Compact Yttria-Stabilized Zirconia Based Total NO_x Sensor with a Dual Functional Co_3O_4/NiO Sensing Electrode, *ACS Sens.*, 2019, **4**, 2150–2155.

24 H. Bi, Y. Shen, S. Zhao, P. Zhou, S. Gao, B. Cui, D. Wei, Y. Zhang and K. Wei, Synthesis of NiO-In_2O_3 heterojunction nanospheres for highly selective and sensitive detection of ppb-level NO_2, *Vacuum*, 2020, **172**, 109086.

25 R. N. Dhanawade, N. S. Pawar, M. A. Chougule, G. M. Hingangavkar, Y. M. Jadhav, T. M. Nimbalkar, Y. H. Navale, G. T. Chavan, C.-W. Jeon and V. B. Patil,

26 K. Mahendraprabhu and P. Elumalai, Stabilized zirconia-based selective NO_2 sensor using sol-gel derived Nb_2O_5 sensing-electrode, *Sens. Actuators, B*, 2017, **238**, 105–110.

27 Y. H. Navale, S. T. Navale, F. J. Stadler, N. S. Ramgir, A. K. Debnath, S. C. Gadkari, S. K. Gupta, D. K. Aswal and V. B. Patil, Thermally evaporated copper oxide films: A view of annealing effect on physical and gas sensing properties, *Ceram. Int.*, 2017, **43**, 7057–7064.

28 M. M. Gomaa, M. H. Sayed, V. L. Patil, M. Boshta and P. S. Patil, Gas sensing performance of sprayed NiO thin films toward NO_2 gas, *J. Alloys Compd.*, 2021, **885**, 160908.

29 S. M. Ingole, S. T. Navale, Y. H. Navale, D. K. Bandgar, F. J. Stadler, R. S. Mane, N. S. Ramgir, S. K. Gupta, D. K. Aswal and V. B. Patil, Nanostructured tin oxide films: Physical synthesis, characterization, and gas sensing properties, *J. Colloid Interface Sci.*, 2017, **493**, 162–170.

30 P. Zhou, Y. Shen, W. Lu, S. Zhao, T. Li, X. Zhong, B. Cui, D. Wei and Y. Zhang, Highly selective NO_2 chemiresistive gas sensor based on hierarchical In_2O_3 microflowers grown on clinoptilolite substrates, *J. Alloys Compd.*, 2020, **828**, 154395.

31 T. M. Nimbalkar, Y. M. Jadhav, R. N. Dhanawade, N. S. Pawar, A. C. Molane, S. S. Gavande, G. T. Chavan, C.-W. Jeon, S. D. Sartale and V. B. Patil, Simple chemical synthesis of CeO_2 nanoparticles for toxic NO_2 gas detection, *J. Alloys Compd.*, 2023, **966**, 171461.

32 G. M. Hingangavkar, Y. H. Navale, T. M. Nimbalkar, R. N. Mulik and V. B. Patil, Hydrothermally engineered WO_3 nanoflowers: A selective detection towards toxic NO_2 gas, *Sens. Actuators, B*, 2022, **371**, 132584.

33 G. M. Hingangavkar, S. A. Kadam, Y.-R. Ma, S. D. Sartale, R. N. Mulik and V. B. Patil, Intercalation of two-dimensional graphene oxide in WO_3 nanoflowers for NO_2 sensing, *Nano-Struct. Nano-Objects*, 2023, **34**, 100964.

34 L. Liu, S. Fu, X. Lv, L. Yue, L. Fan, H. Yu, X. Gao, W. Zhu, W. Zhang, X. Li and W. Zhu, A Gas Sensor With Fe_2O_3 Nanospheres Based on Trimethylamine Detection for the Rapid Assessment of Spoilage Degree in Fish, *Front. Bioeng. Biotechnol.*, 2020, **8**, 567584.

35 A. Król-Górniak, V. Railean, P. Pomastowski, T. Płociński, M. Gloc, R. Dobrucka, K. J. Kurzydłowski and B. Buszewski, Comprehensive study upon physicochemical properties of bio-ZnO NCs, *Sci. Rep.*, 2023, **13**, 587.

36 R. Devi Chandra and K. G. Gopchandran, Simple, Low-Temperature Route To Synthesize ZnO Nanoparticles and Their Optical Neuromorphic Characteristics, *ACS Appl. Electron. Mater.*, 2021, **3**, 3846–3854.

37 H.-J. Kim and J.-H. Lee, Highly sensitive and selective gas sensors using p-type oxide semiconductors: Overview, *Sens. Actuators, B*, 2014, **192**, 607–627.

38 V. V. Volkov, D. J. Oliver and C. C. Perry, Polariton condensation and surface enhanced Raman in spherical ZnO microcrystals, *Nat. Commun.*, 2020, **11**, 4908.

Highly sensitive and selective PAni-CeO_2 nanohybrid for detection of NH_3 biomarker at room temperature, *J. Mater. Sci.: Mater. Electron.*, 2023, **34**, 781.

39 J. Nasser, K. Steinke and H. Sodano, ZnO Nanostructured Interphase for Multifunctional and Lightweight Glass Fiber Reinforced Composite Materials under Various Loading Conditions, *ACS Appl. Nano Mater.*, 2020, **3**, 1363–1372.

40 L. Maria Jose, S. Anna Thomas, A. Aravind, Y.-R. Ma and S. Anil Kadam, Effect of Ni doping on the adsorption and visible light photocatalytic activity of ZnO hexagonal nanorods, *Inorg. Chem. Commun.*, 2023, **147**, 110208.

41 N. S. George, S. Anil Kadam, S. Sreehari, L. Maria Jose, Y. Ron Ma and A. Aravind, Inquest on photocatalytic and antibacterial traits of low composition Cu doped ZnO nanoparticles, *Chem. Phys. Lett.*, 2023, **815**, 140351.

42 M. A. Patil, V. V. Ganbavle, K. Y. Rajpure, H. P. Deshmukh and S. H. Mujawar, Fast response and highly selective nitrogen dioxide gas sensor based on Zinc Stannate thin films, *Mater. Sci. Energy Technol.*, 2020, **3**, 36–42.

43 G. J. Thangamani, K. Deshmukh, T. Kovářík, N. A. Nambiraj, D. Ponnamma, K. K. Sadasivuni, H. P. S. A. Khalil and S. K. K. Pasha, Graphene oxide nanocomposites based room temperature gas sensors: A review, *Chemosphere*, 2021, **280**, 130641.

44 S. Tyagi, M. Chaudhary, A. K. Ambedkar, K. Sharma, Y. K. Gautam and B. P. Singh, Metal oxide nanomaterial-based sensors for monitoring environmental NO_2 and its impact on the plant ecosystem: a review, *Sens. Diagn.*, 2022, **1**, 106–129.

45 Y. H. Navale, S. T. Navale, N. S. Ramgir, F. J. Stadler, S. K. Gupta, D. K. Aswal and V. B. Patil, Zinc oxide hierarchical nanostructures as potential NO_2 sensors, *Sens. Actuators, B*, 2017, **251**, 551–563.

46 S. M. Mali, S. S. Narwade, Y. H. Navale, S. B. Tayade, R. V. Digraskar, V. B. Patil, A. S. Kumbhar and B. R. Sathe, Heterostructural CuO–ZnO Nanocomposites: A Highly Selective Chemical and Electrochemical NO_2 Sensor, *ACS Omega*, 2019, **4**, 20129–20141.

47 N. S. Harale, A. S. Kamble, N. L. Tarwal, I. S. Mulla, V. K. Rao, J. H. Kim and P. S. Patil, Hydrothermally grown ZnO nanorods arrays for selective NO_2 gas sensing: Effect of anion generating agents, *Ceram. Int.*, 2016, **42**, 12807–12814.

48 J. Zhang, X. Liu, G. Neri and N. Pinna, Nanostructured Materials for Room-Temperature Gas Sensors, *Adv. Mater.*, 2016, **28**, 795–831.

49 N. Joshi, T. Hayasaka, Y. Liu, H. Liu, O. N. Oliveira and L. Lin, A review on chemiresistive room temperature gas sensors based on metal oxide nanostructures, graphene and 2D transition metal dichalcogenides, *Microchim. Acta*, 2018, **185**, 213.

50 Q. Yu, C. Yu, J. Wang, F. Guo, S. Gao, S. Jiao, H. Li, X. Zhang, X. Wang, H. Gao, H. Yang and L. Zhao, Gas sensing properties of self-assembled ZnO nanotube bundles, *RSC Adv.*, 2013, **3**, 16619–16625.

51 N. Kaur, M. Singh and E. Comini, One-Dimensional Nanostructured Oxide Chemoresistive Sensors, *Langmuir*, 2020, **36**, 6326–6344.

52 Q. Zhang, G. Xie, M. Duan, Y. Liu, Y. Cai, M. Xu, K. Zhao, H. Tai, Y. Jiang and Y. Su, Zinc Oxide Nanorods for Light-Activated Gas Sensing and Photocatalytic Applications, *ACS Appl. Nano Mater.*, 2023, **6**, 17445–17456.

53 H. Wang, J. Bai, M. Dai, K. Liu, Y. Liu, L. Zhou, F. Liu, F. Liu, Y. Gao, X. Yan and L. Geyu, Visible light activated excellent $NO2$ sensing based on 2D/2D ZnO/g-C_3N_4 heterojunction composites, *Sens. Actuators, B*, 2020, **304**, 127287.

54 Y. Qu, Z. Song and J. Zhang, Enhanced gas-sensing to low-concentration ethanol gas from 3-dimensional (3D) urchin-like ZnO micro/nanospheres, *Mater. Lett.*, 2023, **335**, 133817.

55 J. X. Wang, X. W. Sun, Y. Yang and C. M. L. Wu, N–P transition sensing behaviors of ZnO nanotubes exposed to NO_2 gas, *Nanotechnology*, 2009, **20**, 465501.

56 R. Kumar, O. Al-Dossary, G. Kumar and A. Umar, Zinc Oxide Nanostructures for NO2 Gas–Sensor Applications: A Review, *Nano-Micro Lett.*, 2015, **7**, 97–120.

57 S. Sakalley, A. Saravanan, D. Kathiravan, J.-C. Tang, W.-C. Cheng, S.-C. Chen, H. Sun and B.-R. Huang, Enhanced hydrogen gas sensing through the utilization of a hybrid nanostructure combining ZnO nanotubes and HiPIMS Cu_3N thin film, *Sens. Actuators, B*, 2024, **402**, 135107.

58 V. S. Bhati, M. Hojamberdiev and M. Kumar, Enhanced sensing performance of ZnO nanostructures-based gas sensors: A review, *Energy Rep.*, 2020, **6**, 46–62.

59 M. A. Franco, P. P. Conti, R. S. Andre and D. S. Correa, A review on chemiresistive ZnO gas sensors, *Sens. Actuators Rep.*, 2022, **4**, 100100.

60 G. M. Hingangavkar, S. A. Kadam, Y.-R. Ma, R. N. Mulik and V. B. Patil, Highly selective and sensitive MoS_2 nano-sensor for H_2S detection, *J. Alloys Compd.*, 2023, **941**, 168849.

61 T. J. Trivedi, D. Bhattacharjya, J.-S. Yu and A. Kumar, Functionalized Agarose Self-Healing Ionogels Suitable for Supercapacitors, *ChemSusChem*, 2015, **8**, 3294–3303.

62 B. Zhou, Q. Ma, C. Cui, S. Ma, J. Bai and H. Wang, Preparation of the lead-free graphene-glass frit composites for crystalline silicon solar cells and investigation of performance, *Sol. Energy*, 2020, **211**, 988–998.

63 D. Das and P. Mondal, Photoluminescence phenomena prevailing in c-axis oriented intrinsic ZnO thin films prepared by RF magnetron sputtering, *RSC Adv.*, 2014, **4**, 35735–35743.

64 G. Deroubaix and P. Marcus, X-ray photoelectron spectroscopy analysis of copper and zinc oxides and sulphides, *Surf. Interface Anal.*, 1992, **18**, 39–46.

65 P. Ji, X. Hu, R. Tian, H. Zheng, J. Sun, W. Zhang and J. Peng, Atom-economical synthesis of ZnO@ZIF-8 core–shell heterostructure by dry gel conversion (DGC) method for enhanced H_2 sensing selectivity, *J. Mater. Chem. C*, 2020, **8**, 2927–2936.

66 R. Al-Gaashani, S. Radiman, A. R. Daud, N. Tabet and Y. Al-Douri, XPS and optical studies of different morphologies of ZnO nanostructures prepared by microwave methods, *Ceram. Int.*, 2013, **39**, 2283–2292.

67 C. Yuan, J. Ma, Y. Zou, G. Li, H. Xu, V. V. Sysoev, X. Cheng and Y. Deng, Modeling Interfacial Interaction between Gas Molecules and Semiconductor Metal Oxides: A New View Angle on Gas Sensing, *Adv. Sci.*, 2022, **9**, 2203594.

68 N. K. Chowdhury and B. Bhowmik, Micro/nanostructured gas sensors: the physics behind the nanostructure growth, sensing and selectivity mechanisms, *Nanoscale Adv.*, 2021, **3**, 73–93.

69 J.-H. Kim, Y. Zheng, A. Mirzaei and S. Kim, Excellent Carbon Monoxide Sensing Performance of Au-Decorated SnO_2 Nanofibers, *Korean J. Mater. Res.*, 2016, **26**, 741–750.

70 J.-H. Kim, A. Mirzaei, H. W. Kim and S. S. Kim, Low-Voltage-Driven Sensors Based on ZnO Nanowires for Room-Temperature Detection of NO_2 and CO Gases, *ACS Appl. Mater. Interfaces*, 2019, **11**, 24172–24183.

71 X. Li, Z. Zhuang, D. Qi and C. Zhao, High sensitive and fast response humidity sensor based on polymer composite nanofibers for breath monitoring and non-contact sensing, *Sens. Actuators, B*, 2021, **330**, 129239.

72 H.-S. Kim, J.-H. Kang, J.-Y. Hwang and U. S. Shin, Wearable CNTs-based humidity sensors with high sensitivity and flexibility for real-time multiple respiratory monitoring, *Nano Convergence*, 2022, **9**, 35.

73 S. Kanaparthi and S. G. Singh, Reduction of the Measurement Time of a Chemiresistive Gas Sensor Using Transient Analysis and the Cantor Pairing Function, *ACS Meas. Sci. Au*, 2022, **2**, 113–119.

74 M. Al-Hashem, S. Akbar and P. Morris, Role of Oxygen Vacancies in Nanostructured Metal-Oxide Gas Sensors: A Review, *Sens. Actuators, B*, 2019, **301**, 126845.

75 J. Xuan, G. Zhao, M. Sun, F. Jia, X. Wang, T. Zhou, G. Yin and B. Liu, Low-temperature operating ZnO-based NO_2 sensors: a review, *RSC Adv.*, 2020, **10**, 39786–39807.

76 J. Sukunta, A. Wisitsoraat, A. Tuantranont, S. Phanichphant and C. Liewhiran, WO3 nanotubes−SnO_2 nanoparticles heterointerfaces for ultrasensitive and selective NO2 detections, *Appl. Surf. Sci.*, 2018, **458**, 319–332.

77 Z. Chen, H. Guo, F. Zhang, X. Li, J. Yu and X. Chen, Porous ZnO/rGO Nanosheet-Based NO_2 Gas Sensor with High Sensitivity and ppb-Level Detection Limit at Room Temperature, *Adv. Mater. Interfaces*, 2021, **8**, 2101511.

78 A. Afzal, N. Cioffi, L. Sabbatini and L. Torsi, NO_x sensors based on semiconducting metal oxide nanostructures: Progress and perspectives, *Sens. Actuators, B*, 2012, **171–172**, 25–42.

79 V. Balasubramani, S. Chandraleka, T. S. Rao, R. Sasikumar, M. R. Kuppusamy and T. M. Sridhar, Review—Recent Advances in Electrochemical Impedance Spectroscopy Based Toxic Gas Sensors Using Semiconducting Metal Oxides, *J. Electrochem. Soc.*, 2020, **167**, 037572.

80 V. Balasubramani, S. Sureshkumar, T. S. Rao and T. M. Sridhar, Impedance Spectroscopy-Based Reduced Graphene Oxide-Incorporated ZnO Composite Sensor for H2S Investigations, *ACS Omega*, 2019, **4**, 9976–9982.

81 P. Sobaś, O. Nilsen, H. Fjellvåg and B. Svensson, Electrical Properties and Gas Sensing Characteristics of the Al_2O_3/4H SiC Interface Studied by Impedance Spectroscopy, *Mater. Sci. Forum*, 2010, 531–534.

82 G. M. Hingangavkar, S. A. Kadam, Y.-R. Ma, S. S. Bandgar, R. N. Mulik and V. B. Patil, Tailored formation of WO3-rGO nanohybrids for dependable low temperature NO_2 sensing, *Ceram. Int.*, 2023, **49**, 38866–38876.

83 G. M. Hingangavkar, S. A. Kadam, Y.-R. Ma, S. S. Bandgar, R. N. Mulik and V. B. Patil, MoS_2-GO hybrid sensor: A discerning approach for detecting harmful H_2S gas at room temperature, *Chem. Eng. J.*, 2023, **472**, 144789.

84 S. B. Kulkarni, Y. H. Navale, S. T. Navale, F. J. Stadler, N. S. Ramgir and V. B. Patil, Hybrid polyaniline-WO_3 flexible sensor: A room temperature competence towards NH_3 gas, *Sens. Actuators, B*, 2019, **288**, 279–288.

85 D. K. Bandgar, S. T. Navale, S. R. Nalage, R. S. Mane, F. J. Stadler, D. K. Aswal, S. K. Gupta and V. B. Patil, Simple and low-temperature polyaniline-based flexible ammonia sensor: a step towards laboratory synthesis to economical device design, *J. Mater. Chem. C*, 2015, **3**, 9461–9468.

86 G. M. Hingangavkar, S. A. Kadam, Y.-R. Ma, M. Selvaraj, R. N. Mulik and V. B. Patil, On the behavior of MoS_2-rGO nanocomposites for chemiresistive H_2S detection at room temperature, *Sens. Actuators, B*, 2024, **399**, 134843.

87 S. A. Kadam, Y.-R. Ma, Y.-R. Chen, Y. H. Navale, A. S. Salunkhe, V. B. Patil, S. D. Ralegankar and P. D. More, Mn-Incorporated α-Fe_2O_3 Nanostructured Thin Films: Facile Synthesis and Application as a High-Performance Supercapacitor, *J. Electron. Mater.*, 2023, **52**, 500–513.

88 Y. Su, W. Li, X. Cheng, Y. Zhou, S. Yang, X. Zhang, C. Chen, T. Yang, H. Pan, G. Xie, G. Chen, X. Zhao, X. Xiao, B. Li, H. Tai, Y. Jiang, L.-Q. Chen, F. Li and J. Chen, High-performance piezoelectric composites via β phase programming, *Nat. Commun.*, 2022, **13**, 4867.

89 X. Yang, Y. Deng, H. Yang, Y. Liao, X. Cheng, Y. Zou, L. Wu and Y. Deng, Functionalization of Mesoporous Semiconductor Metal Oxides for Gas Sensing: Recent Advances and Emerging Challenges, *Adv. Sci.*, 2023, **10**, 2204810.

90 T. V. A. Kusumam, V. S. Siril, K. N. Madhusoodanan, M. Prashantkumar, Y. T. Ravikiran and N. K. Renuka, NO_2 gas sensing performance of zinc oxide nanostructures synthesized by surfactant assisted Low temperature hydrothermal technique, *Sens. Actuators, A*, 2021, **318**, 112389.

91 R. C. Pawar, J.-W. Lee, V. B. Patil and C. S. Lee, Synthesis of multi-dimensional ZnO nanostructures in aqueous medium for the application of gas sensor, *Sens. Actuators, B*, 2013, **187**, 323–330.

92 Y. Xia, L. Zhou, J. Yang, P. Du, L. Xu and J. Wang, Highly Sensitive and Fast Optoelectronic Room-Temperature NO_2 Gas Sensor Based on ZnO Nanorod-Assembled Macro-/Mesoporous Film, *ACS Appl. Electron. Mater.*, 2020, **2**, 580–589.

93 X. Chen, Y. Shen, W. Zhang, J. Zhang, D. Wei, R. Lu, L. Zhu, H. Li and Y. Shen, In-situ growth of ZnO nanowire arrays on the sensing electrode via a facile hydrothermal route for high-performance NO_2 sensor, *Appl. Surf. Sci.*, 2018, **435**, 1096–1104.

94 X. Liu, Q. Li, Y. Cui, J. Lin and L. Ding, Synthesis of porous spherical ZnO nanomaterials and the selective detection of NO at room temperature, *Sens. Actuators, B*, 2023, **378**, 133155.

95 J. Fang, J.-J. Xue, R.-P. Xiao, X. Chen, Y.-M. Guo and J.-M. Song, Synthesis of Pr-doped ZnO nanospindles by one-pot precipitation as a triethylamine sensor, *J. Environ. Chem. Eng.*, 2022, **10**, 108334.

96 Y. Li, Y. Liu, Y. Lu, Z. Liu, C. Sui, Y. Wang, L. Yang, F. Liu, P. Sun, F. Liu and G. Lu, Preparation of BiOI-Functionalized ZnO Nanorods for Ppb-Level NO2 Detection at Room Temperature, *ACS Sens.*, 2022, **7**, 3915–3922.

97 N. A. Isaac, I. Pikaar and G. Biskos, Metal oxide semiconducting nanomaterials for air quality gas sensors: operating principles, performance, and synthesis techniques, *Microchim. Acta*, 2022, **189**, 196.